Classification of Tropical Oceanic Precipitation using High-Altitude Aircraft Microwave and Electric Field Measurements

ROBBIE E. HOOD,* DANIEL J. CECIL,[+] FRANK J. LAFONTAINE,[#] RICHARD J. BLAKESLEE,*
DOUGLAS M. MACH,[+] GERALD M. HEYMSFIELD,[@] FRANK D. MARKS JR.,[&] EDWARD J. ZIPSER,**
AND MICHAEL GOODMAN*

*NASA Marshall Space Flight Center, Huntsville, Alabama
[+]University of Alabama in Huntsville, Huntsville, Alabama
[#]Raytheon Technical Services Company, Huntsville, Alabama
[@]NASA Goddard Space Flight Center, Greenbelt, Maryland
[&]NOAA/Hurricane Research Division, Miami, Florida
**University of Utah, Salt Lake City, Utah

ABSTRACT

During the 1998 and 2001 hurricane seasons of the western Atlantic Ocean and Gulf of Mexico, the Advanced Microwave Precipitation Radiometer (AMPR), the ER-2 Doppler (EDOP) radar, and the Lightning Instrument Package (LIP) were flown aboard the NASA ER-2 high-altitude aircraft as part of the Third Convection and Moisture Experiment (CAMEX-3) and the Fourth Convection and Moisture Experiment (CAMEX-4). Several hurricanes, tropical storms, and other precipitation systems were sampled during these experiments. An oceanic rainfall screening technique has been developed using AMPR passive microwave observations of these systems collected at frequencies of 10.7, 19.35, 37.1, and 85.5 GHz. This technique combines the information content of the four AMPR frequencies regarding the gross vertical structure of hydrometeors into an intuitive and easily executable precipitation mapping format. The results have been verified using vertical profiles of EDOP reflectivity and lower-altitude horizontal reflectivity scans collected by the NOAA WP-3D Orion radar. Matching the rainfall classification results with coincident electric field information collected by the LIP readily identifies convective rain regions within the precipitation fields. This technique shows promise as a real-time research and analysis tool for monitoring vertical updraft strength and convective intensity from airborne platforms such as remotely operated or uninhabited aerial vehicles. The technique is analyzed and discussed for a wide variety of precipitation types using the 26 August 1998 observations of Hurricane Bonnie near landfall.

1. Introduction

A crucial need exists to understand and map the precipitation types, patterns, and variations of a tropical cyclone (TC) in order to develop better skill in quantitative precipitation estimation necessary for more accurate forecasts of rainfall impacts during landfalling tropical storms and hurricanes. Identification of rainfall patterns, vertical hydrometeor profiles, and corresponding vertical motions are also necessary for defin-

ing latent heat profiles and regions of convective strength, which in turn can be used to improve hurricane intensity change forecasting as well as general numerical weather prediction.

In an effort to examine how these issues might be addressed through better utilization of remotely sensed observations from spaceborne or airborne platforms, the National Aeronautics and Space Administration (NASA) sponsored the Third Convection and Moisture Experiment (CAMEX-3) in 1998 and the Fourth Convection and Moisture Experiment (CAMEX-4) in 2001 (Kakar et al. 2006). Several hurricanes, tropical storms, and other precipitation systems in the western Atlantic and Gulf of Mexico were sampled during these field campaigns yielding a comprehensive volume of infor-

Corresponding author address: Robbie E. Hood, Earth and Planetary Science Branch (Code XD11), NASA Marshall Space Flight Center, Huntsville, AL 35812.
E-mail: Robbie.Hood@nasa.gov

mation collected by satellite, aircraft, and ground-based instrumentation. The primary NASA aircraft were the high-altitude ER-2 and medium-altitude DC-8. A collaborative partnership with the Hurricane Research Division of the National Oceanic and Atmospheric Administration (NOAA) also provided opportunities for joint missions with the NOAA WP-3D Orion (P-3) aircraft.

Using data collected during CAMEX-3 and CAMEX-4, this study examines the relationship of three key sets of observations and the information they jointly provide regarding vertical precipitation profiles and convective intensity for tropical precipitation systems. In particular, this study explores how to optimally combine the information content of the multifrequency mapping of passive microwave brightness temperatures provided by the Advanced Microwave Precipitation Radiometer (AMPR), the vertical profiling of radar reflectivity provided by the ER-2 Doppler (EDOP) radar, and the cloud electric field vectors provided by the Lightning Instrument Package (LIP). The synergy of these observations highlights the type and convective strength of the TC precipitation elements sampled in the western Atlantic and Gulf of Mexico.

Previous efforts to identify precipitation characteristics of tropical cyclones have included extensive analysis of microwave remote sensing information. Wilheit et al. (1982) discussed the correlation of increasing 19.35-GHz and decreasing 92-GHz passive microwave brightness temperatures to increasing rain rates using aircraft observations of Tropical Storm Cora. Marks (1985) used aircraft radar reflectivities collected during Hurricane Allen in 1980 to examine the relationship of storm intensity change to rain rate and total rainfall. Spencer et al. (1994) and McGaughey et al. (1996) presented different aspects of passive microwave aircraft observations of TC Oliver collected by the AMPR during 4–9 February 1993 in the western Pacific as part of the Tropical Ocean and Global Atmosphere Coupled Ocean–Atmosphere Response Experiment (TOGA COARE). Spencer et al. (1994) presented the first high resolution, multifrequency passive microwave imagery of a TC during their description of the AMPR sampling capabilities. McGaughey et al. (1996) explored multifrequency passive microwave signatures of tropical oceanic precipitation systems. They explained the spatial shift of lower-altitude rain emission microwave signatures from higher-altitude ice scattering microwave signatures as a result of the tilt with height of convective elements in the eyewall of TC Oliver. Tilted convective elements within Hurricane Bonnie on 25 August 1998 in the western Atlantic Ocean have also been identified

by Hong et al. (2000) using Tropical Rainfall Measuring Mission (TRMM) Microwave Imager (TMI) and Special Sensor Microwave Imager (SSM/I) satellite observations.

Other investigations have studied the role of lightning to signal TC intensity change or the relationship of lightning with other precipitation parameters. Simpson et al. (1998) explored cloud electrification and lightning linked to the vertical radar structure and other features of the clouds in a study of cyclogenesis in TOGA COARE associated with TC Oliver. Molinari et al. (1999) correlated the occurrence of eyewall lightning measured by a ground-based detection network with the beginning and continuation of TC intensification. Cecil and Zipser (1999) examined the relationship of satellite observations of passive 85.5-GHz ice scattering signatures and lightning in TC eyewalls and rainbands to future TC intensity change. Cecil and Zipser (2002) examined relationships between satellite passive microwave, radar, and lightning inferring microphysical characteristics of eyewalls and rainbands.

The primary purpose of this study is to demonstrate a methodology to merge the information content of AMPR, EDOP, and LIP observations, each of which have a different spatial context. This leads to a rainfall screening technique using AMPR passive microwave observations. The screening technique is verified using vertical profiles of EDOP reflectivity and lower-altitude horizontal reflectivity scans collected by the NOAA P-3 radar. A unique aspect of our study is that the LIP observations provide a means to examine the trends of electric field in relation to convective activity instead of relying on the occurrence of lightning, which is not frequent in tropical oceanic storms. Matching the rainfall classification with coincident electric field information collected by the LIP readily identifies convective rain regions within TC precipitation fields.

Descriptions of the instruments are presented in section 2. The AMPR screening method as well as the EDOP verification and coincident LIP data are presented in section 3. An illustration is presented in section 4 using a portion of Hurricane Bonnie data collected on 26 August 1998 that displays a wide variety of precipitation structures. The Hurricane Bonnie illustration is also a proof of concept of a real-time analysis tool for monitoring vertical updraft strength and convective intensity from a remotely operated or uninhabited aerial vehicle. These types of vehicles are likely components of a future network of spaceborne, suborbital, and ground-based earth observing platforms combining the advantages of each platform for flexible,

adaptive sampling of critical weather events such as tropical storms and hurricanes.

2. Instrument descriptions

a. The Advanced Microwave Precipitation Radiometer

The AMPR is a total power passive microwave radiometer producing calibrated brightness temperatures (TBs) at 10.7, 19.35, 37.1, and 85.5 GHz. These frequencies are sensitive to the emission and scattering of precipitation-sized ice, liquid water, and water vapor. The AMPR performs a 90° cross-track data scan perpendicular to the direction of aircraft motion. It processes a linear polarization feed with full vertical polarization at $-45°$ and full horizontal polarization at $+45°$, with the polarization across the scan mixed as a function of $\sin^2$, giving an equal V–H mixture at 0° (aircraft nadir). A full calibration is made every fifth scan using hot and cold blackbodies. From a typical ER-2 flight altitude of ~20 km, surface footprint sizes range from 640 m (85.5 GHz) to 2.8 km (10.7 GHz). All four channels share a common measurement grid with collocated footprint centers, resulting in oversampling of the low frequency channels with respect to 85.5 GHz. A more complete description of the instrument may be found in Spencer et al. (1994).

An example of AMPR TB imagery is presented in Fig. 1 for a portion of Hurricane Bonnie on 26 August 1998. The false color scale chosen for this imagery ranges from magenta and blue colors for cold TB to yellow and red colors for warm TB. In general, land surfaces and rain are radiometrically warm while the ocean is radiometrically cold because of their respective microwave emission properties. Precipitation ice may also appear as a radiometrically cold signature for a given frequency because ice tends to scatter upwelling microwave energy out of the instrument's field of view unless the diameter of ice particles is small compared to the wavelength. See Wilheit et al. (1977), Wu and Weinman (1984), Wilheit (1986), and Spencer et al. (1989) for further explanation.

In Fig. 1, the 10.7-GHz information delineates rain and rain-free regions with warmer TB representing increasing rain rates. The 19.35-GHz information also serves this purpose but with a smaller dynamic range than the 10.7 GHz (Smith et al. 1994). The 19.35-GHz frequency is more sensitive to clouds and ice than the 10.7 GHz. In the image, the 37.1-GHz information displays a similar sensitivity to clouds as the 19.35-GHz frequency, but the 37.1-GHz frequency is more sensitive to smaller size ice. The coldest 37.1-GHz TB in this image represent clear-sky regions over a radiometri-cally cold ocean background such as in the eye near 33.2°N, 77.8°W. In the 85.5-GHz image, water vapor, clouds, and smaller ice are very noticeable. Precipitation ice is colder than the surrounding rain and cloud. Regions of blues and greens (e.g., at 32.6°N, 77.4°W) indicate large quantity and/or mass of ice. Note that the eye is almost obscured at this frequency probably due to thin clouds and/or high water vapor content. The spray of small dots found in Fig. 1 corresponds to geolocation during aircraft turns.

b. The ER-2 Doppler radar

The EDOP operates at 9.6 GHz providing high resolution (i.e., 37.5 m vertical, with the horizontal footprint varying from about 400 m at the tropopause level to 1.2 km at the surface) time–height sections of reflectivity and vertical hydrometeor velocity in the vertical plane mapped out by the ER-2 (Heymsfield et al. 2001). It is nonscanning with one nadir beam and one forward beam, although only the nadir beam is used here. Vertical air motions are also retrieved when the hydrometeor fall speed and aircraft motions are removed. EDOP reflectivities are calibrated to within approximately 1 dB. These have been verified using various approaches including the use of the ocean backscatter and comparison with the TRMM precipitation radar and ground-based radars. The minimal detectable signal is approximately -15 dBZ near cirrus cloud top and 0 dBZ near the surface. A more complete description of the EDOP and its other capabilities (e.g., ability to measure linear depolarization ratio, dual Doppler retrieval along the flight track) may be found in Heymsfield et al. (1996).

c. The Lightning Instrument Package

The LIP consists of eight state-of-the-art, low-noise, high dynamic range electric field mills on the aircraft (three mills per instrument superpod mounted on each wing and two on the fuselage). With these sensors, the full vector components of the atmospheric electric field (i.e., Ex, Ey, Ez) are obtained, providing detailed information about the electric structure within and around the storms overflown. The field mills measure the components of the electric field over a wide dynamic range extending from fair weather electric fields (i.e., a few volts per meter) to large thunderstorm fields (i.e., tens of kilovolts per meter). The set of equations that relate the field mill outputs to the atmospheric electric field is determined by an iterative calibration process (Mach and Koshak 2003). Total lightning (i.e., intracloud and cloud to ground) is identified from the abrupt changes in the electric field data.
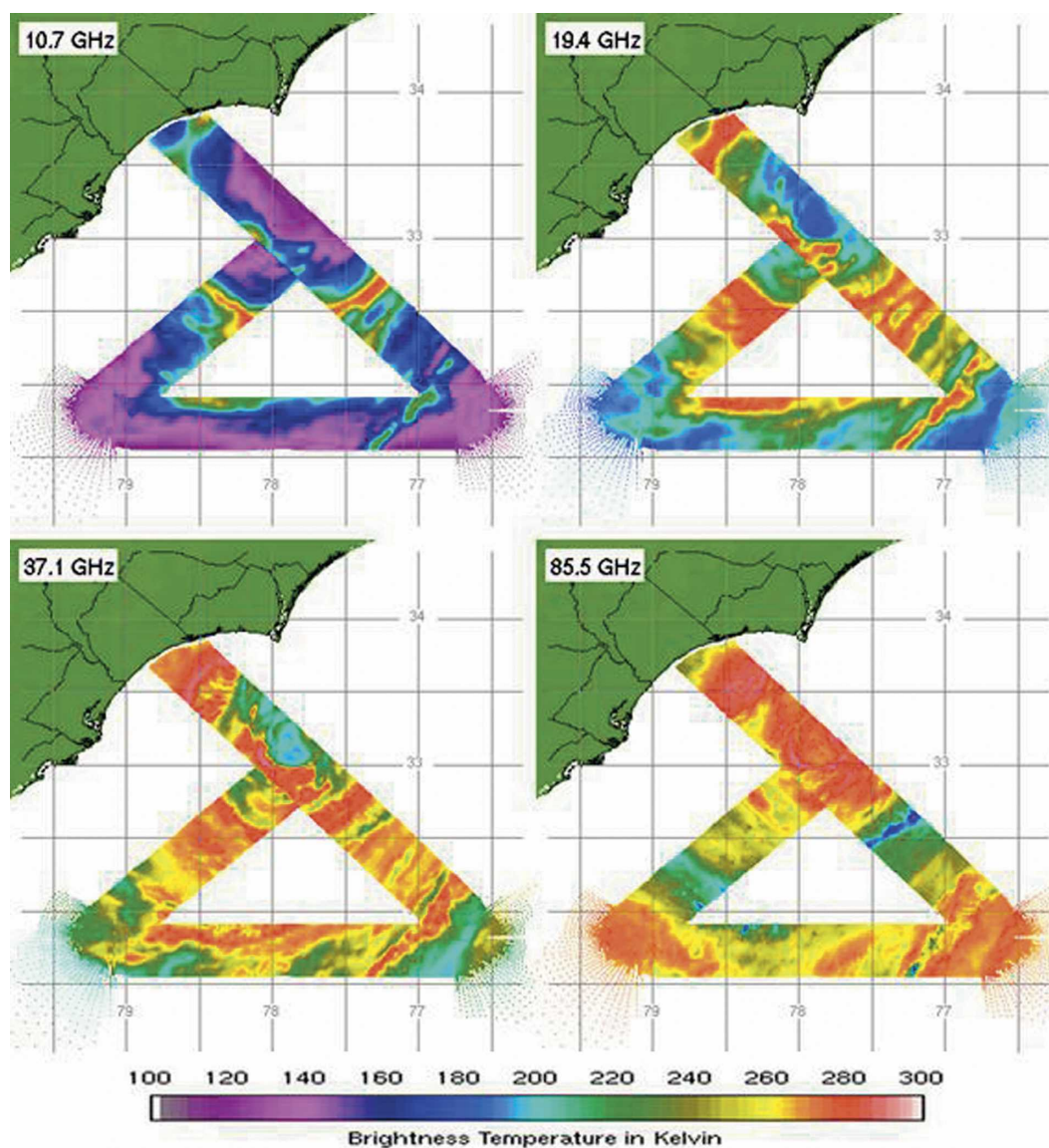
FIG. 1. AMPR brightness temperatures at 10.7, 19.35, 37.1, and 85.5 GHz for Hurricane Bonnie at 1500–1600 UTC on 26 Aug 1998. Low brightness temperatures are magenta and blue; high brightness temperatures are yellow and red. Swath width is approximately 40 km at the surface.

3. Method of analysis

a. Precipitation classification using AMPR

An AMPR precipitation index (API) has been developed that utilizes the brightness temperature information for precipitation and clouds over the ocean at the four frequencies to produce a single index value at each AMPR footprint. The goal of the API development is to combine the information content of the four frequencies into an intuitive format that readily identifies the gross vertical structure of the hydrometeors at a given pixel location based on the microwave emission by the rain and scattering by the ice. The method is not meant to be a replacement for the iterative hydrometeor retrieval of Skofronick-Jackson et al. (2003), the texture-polarization method of Olson et al. (2001), or a Bayesian approach. The Skofronick-Jackson retrieval method uses nadir aircraft observations of active and passive microwave sensors and a cloud-resolving model to deduce vertical content and particle size distribution using a computationally intense scheme. The Olson method is a satellite technique for conically scanning passive microwave radiometers that estimates the area coverage of convective and stratiform precipitation us-

TABLE 1. The AMPR precipitation index descriptions, criteria, and representative rain rates are shown below. Criteria for API rain tests vary across-track (see text); the listed values are applicable at nadir. Rain rates were estimated by applying the Jorgensen and Willis (1982) $Z = 300R^{1.35}$ relationship to the median 1-km altitude reflectivity value for each EDOP/AMPR vertical profile. Here, I/η is the fraction of the index to the total of all rain-only samples ($\eta = 231\,042$) and rr_{est} rain rate (mm h^{-1}) estimated at 4-km altitude because of attenuation uncertainty. Ice level 0 (no ice) and levels 4–6 rain do not significantly occur and are included in index 5. Ice level 1 (moderate ice) and level 6 rain does not significantly occur and is included in index 10. Ice level 2 (heavy ice) and level 6 rain does not significantly occur and is included in index 15. Ice level 3 (intense ice) and levels 1–3 rain do not significantly occur and are not included.

API	Description	Criteria	I/η	Rain rate
0	Clear	Tb10 < 160 and Tb37 < 215	n/a	0
1	Moderate cloud	Tb19 > 190 or Tb85 > 260	n/a	0
2	Heavy cloud	Tb85 > 270	n/a	0
Ice level 0		Tb85 < Tb37 and Tb85 < 275		
3	Rain level 1	Tb10 > 160 or Tb37 > 215	0.40	0.4
4	Rain level 2	Tb10 > 175	0.005	5
5	Rain level 3	Tb10 > 200	0.001	7
Ice level 1				
6	Rain level 1	Tb10 > 160 or Tb37 > 215	0.27	2
7	Rain level 2	Tb10 > 175	0.14	5
8	Rain level 3	Tb10 > 200	0.05	8
9	Rain level 4	Tb10 > 225	0.03	13
10	Rain level 5	Tb10 > 250	0.02	19
Ice level 2				
11	Rain level 1	Tb10 > 160 or Tb37 > 215	0.002	3
12	Rain level 2	Tb10 > 175	0.02	4
13	Rain level 3	Tb10 > 200	0.03	7
14	Rain level 4	Tb10 > 225	0.02	13$_{est}$
15	Rain level 5	Tb10 > 250	0.01	19$_{est}$
Ice level 3				
16	Rain level 4	Tb10 > 225	0.001	n/a
17	Rain level 5	Tb10 > 250	0.005	27$_{est}$
18	Rain level 6	Tb10 > 275	0.003	37$_{est}$

ing 85.5-GHz polarization information and lower frequency texture data correlating local maximum signatures to neighboring footprints. The method is not feasible for this study because the AMPR data lack polarization information. The Bayesian method is a computationally efficient technique that can be used to match brightness temperatures to hydrometeor profiles (Kummerow et al. 1996; Evans et al. 1995), given a statistical database of profiles generated a priori by cloud-resolving model profiles.

The API is presented as an alternate approach that is a conceptually and computationally simple method to provide useful qualitative descriptions of the cloud vertical structure found in the extensive precipitation datasets collected by the AMPR during CAMEX-3 and CAMEX-4. The API technique presented here is dependent upon the scanning strategy of the AMPR. It could be readily adapted for other radiometer scanning strategies or expanded to include information from other sensors. While more sophisticated approaches may yield more accurate retrievals, a strength of the API is that any measurement can be related to the physical concepts of microwave emission by rain and scattering by ice.

In general, the API reflects the magnitude (mass) of liquid water and precipitation-sized ice aloft. It is based on physical concepts of microwave rain emission and ice scattering (e.g., Wilheit et al. 1977; Wu and Weinman 1984; Wilheit 1986; Spencer et al. 1989; Smith et al. 1994). The indices are listed in Table 1 along with descriptors and estimated rain rates. The rain rates are presented for illustrative purposes only. The conversion of TB to quantitative rain rate is beyond the scope of this paper. Instead, the emphasis is on initial precipitation screening following the example of Ferraro et al. (1998).

The general approach for the classification is based on four levels of ice scattering and six levels of rain emission. The combinations yield 24 categories of precipitation, in addition to the two cloud categories. Several of the precipitation categories have been combined because the necessary conditions (e.g., strong rain emission without 85.5-GHz scattering, or weak rain emission with 19.35-GHz scattering) occur so rarely. Some rarely occurring categories have been kept separate because their observed radar reflectivity profiles are substantially different from those in categories with which they would be combined.

The API is designed for ocean-only cases that have been screened for large aircraft pitch, roll, and altitude variations that greatly influence the TB values. All pixels within 3.2 km of land are not used to avoid contamination from varying land surface emissions. An API value of 0 indicates that no clouds or rain are detected by AMPR. API values of 1 or 2 suggest the presence of clouds or very light rain, with microwave emissions exceeding 190 K (19.35 GHz) or 260 K (85.5 GHz). The AMPR frequencies are not well suited to detecting some cloud types; so we do not interpret an API value of 0 as indicating truly clear skies.

For API rain values of 3–18, six TB rain emission tests and four TB ice scattering tests are performed. First a rain/no-rain emission test is performed based on 10.7 and 37.1 GHz TBs. The 10.7-GHz channel is used because it is sensitive to emission by rain and least sensitive to cloud water and scattering by ice. The 37.1-GHz channel is used to resolve small-scale features because of its higher spatial resolution. The thresholds for this test are TB10 > 160 K or TB37 > 215 K at nadir. They vary across the scan by up to 53 K for the 10.7-GHz test and 30 K for the 37.1-GHz test to account for the AMPR rotating polarization and varying incidence angle. This across-scan threshold variability is empirically based on the brightness temperatures in several nonraining scans from multiple flights. After this test, the remaining five emission tests check for TB10 exceeding 175, 200, 225, 250, 275 K, indicating increasing liquid water mass and thus inferring increasing rain rates.

The scattering tests indicate which AMPR wavelengths are being scattered by ice. In general, the larger the ice particles that are present, the longer the wavelength that will be scattered. This relationship can be used as a surrogate indicator of vigorous convection. For rain in the absence of appreciable precipitation-sized ice, the higher frequency channels usually have greater TB than the lower frequency channels. In such cases, the precipitation index has values of 3 through 5. If the 85.5-GHz TB is less than 37.1-GHz TB and less than a threshold of 275 K, it is indicating the effects of ice scattering. If only the 85.5-GHz channel is scattered (i.e., ice is large enough to scatter 3.5-mm wavelength radiation), an index of 6 through 10 is assigned. If 37.1-GHz TB is also less than 19.35-GHz TB, we interpret this to mean the ice is large enough to scatter the 37.1-GHz channel (8.1-mm wavelength), and an index of 11 to 15 is assigned. If the ice present is then large enough to scatter the 19.35-GHz TB (1.6-cm wavelength), but not the 10.7-GHz TB an index of 16 to 18 is assigned. The strongest convection (with the largest ice) can scatter the 10.7-GHz TBs, but this is not incorporated into the algorithm because a lower frequency would be required in the current framework.

The classification scheme has been developed based on several late-summer flights over the western Atlantic and the Gulf of Mexico as prescribed. But the rain/no-rain discrimination may be susceptible to varying surface conditions. Rainfall associated with lower brightness temperatures could likely be identified over colder sea surface temperature (SST), and the algorithm would need to be tuned for such instances. A warmer SST may lead to overdetermination of rain, with the emission criteria triggered too often. Roughening of the ocean surface may similarly affect the emission thresholds. One possibility for addressing these issues is to dynamically adjust the rain/no-rain criteria based on observational and/or radiative transfer model retrieved parameters of SST and wind speed.

b. Verification using EDOP information

The API has been compared with EDOP reflectivity profiles for the tropical cyclone and precipitation cases collected during CAMEX-3 and CAMEX-4. This includes missions over Hurricane Bonnie (23, 26 August 1998), Hurricane Earl (2 September 1998), Hurricane Georges (21, 22, 25, 27 September 1998), Hurricane Erin (10 September 2001), Hurricane Humberto (22–24 September 2001), and other convective systems near Florida (5, 17 September 1998; 9, 19 September 2001). For each AMPR scan, the precipitation indices of the middle two (nadir) pixels are matched with the simultaneous nadir reflectivity profile from EDOP. This yields ~80 000 realizations of the vertical profiles associated with the AMPR precipitation indices.

From the set of observed reflectivity profiles, a characteristic (median) profile is assigned to each API. These characteristic profiles are shown in Fig. 2, and are used to produce simulated radar reflectivity from the AMPR measurements. The variability about each characteristic profile is assessed using cumulative density function (CDF) of reflectivity. Such CDFs for some of the most common API values are shown in Fig. 3. Although beyond the scope of this paper, the precipitation index can be applied to various problems after converting to rain rate or ice mass. This can be accomplished by using Figs. 2 and 3 with a radar reflectivity–rain rate (Z–R) or other suitable relationship for a particular application.

The reflectivity profiles verify that the precipitation index provides a measure of the precipitation and clouds in the vertical profile at nadir. When the API identifies neither rain nor cloud, there is usually no
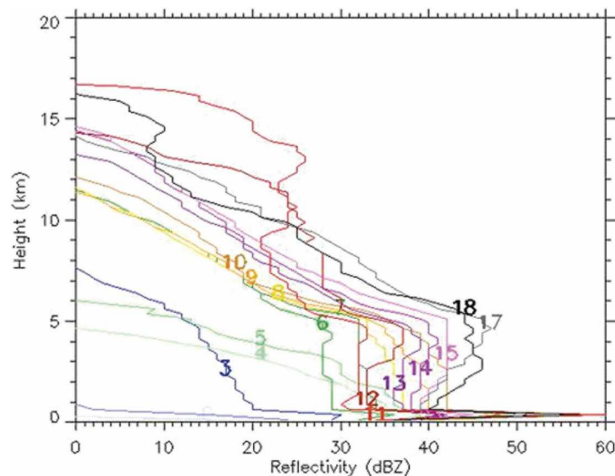
FIG. 2. Vertical profiles of median EDOP reflectivity for all nadir pixels, sorted by API. API = 1 is omitted because it is subzero at all heights. API = 16 is omitted because of insufficient sample size.

reflectivity detected by EDOP in Fig. 3a. Only in rare cases does the reflectivity exceed 10 dBZ. Some non-precipitating clouds go undetected by API, but cloud identification is secondary to our goal of precipitation mapping. The cloud categories (1 and 2) also tend to have low (or subdetectable) reflectivities (Fig. 3b). It is more common to find measurable reflectivity near the surface in category 2 (not shown), suggesting that shallow, very light rain is sometimes included.

The shallow rain categories (3 to 5) do reliably indicate surface precipitation (Figs. 3c,d). These shallow rain profiles sometimes include an ice layer, but with low reflectivity values (i.e., small ice is unable to trigger the larger API categories). The higher 10.7-GHz emission thresholds in categories 4 and 5 result in larger low-level reflectivities from the liquid rain layer (Fig. 2).

Categories 6–10, those having only the 85.5-GHz channel scattered, consistently include an ice layer detectable by EDOP (Figs. 3e,f). The reflectivities often decrease sharply from the liquid layer through the ice layer, indicating that any convection is weak. Radar bright bands are often present (except in category 10) and are indicative of stratiform rain. As intended, the liquid rain rates increase with increasing 10.7-GHz emission thresholds in categories 6–10 (Fig. 2). Reflectivities above the freezing level are similar for each of these categories, because they share the same 85.5-GHz scattering criteria.

Categories 11–15 (i.e., those having the 37.1-GHz channel scattered) consistently have convective profiles with a deep layer of reflectivity greater than 20 dBZ (Fig. 2). Categories 16 to 18 (with the 19.35-GHz chan-

nel scattered) include the strongest convection, with 30+ dBZ radar echoes well above the freezing level (Fig. 2). In this last set of categories (16–18), increasing 10.7-GHz TB no longer distinguish increasing rain rates. Instead, the lower 10.7-GHz thresholds for categories 16 and 17 sometimes distinguish greater scattering by large ice in these categories as compared to category 18. Categories 16 and 17 tend to have stronger convective profiles (greater reflectivity aloft) than category 18 (Fig. 2). This is an unintended result, but enables us to better resolve strong convection. The precipitation mass aloft in these categories attenuates the low-level reflectivities. Even though attenuation has been accounted for following the alpha-adjustment technique (Iguchi and Meneghini 1994), comparison of liquid rain rates between categories 16 to 18 is not reliable.

c. Merger of LIP information

For many years, aircraft have routinely made measurements of electric fields associated with clouds (e.g., Gunn and Parker 1946; Blakeslee et al. 1989; Winn 1993). Some applications of aircraft electric field measurements have been made to the study of tropical cyclones (e.g., Orville et al. 1997; Simpson et al. 1998). For the ER-2, the vector electric field is derived using the outputs measured by the eight electric field mills installed on the aircraft. The set of equations that relate these field mill outputs to the external electric field is represented as a matrix equation. Calibration of the field mill set on an aircraft involves the determination of the matrix coefficients using an iterative process (Mach and Koshak 2003).

For this paper, calibrated electric field data are merged with the AMPR data by projecting the three-dimensional vector electric field onto the aircraft track as seen in Fig. 4. The three line plots Fig. 4 represent the aircraft position projected onto the latitude/longitude, latitude/altitude, or longitude/altitude planes. The API data are mapped only on the latitude/longitude plane. The barbs on the aircraft tracks represent the two-dimensional projection of the vector electric field onto the plane of the plot at selected time intervals. The direction of the barb is the direction of the electric field (in that projection) while the length of the barb corresponds to the magnitude of the vector electric field (again in that projection). The resultant plot indicates the highest fields (where the barbs are the longest), as well as approximately where the sources of the fields are located (direction of the barbs). In general, for simple charge distributions, the electric field will point away (for positive charges) or toward (for
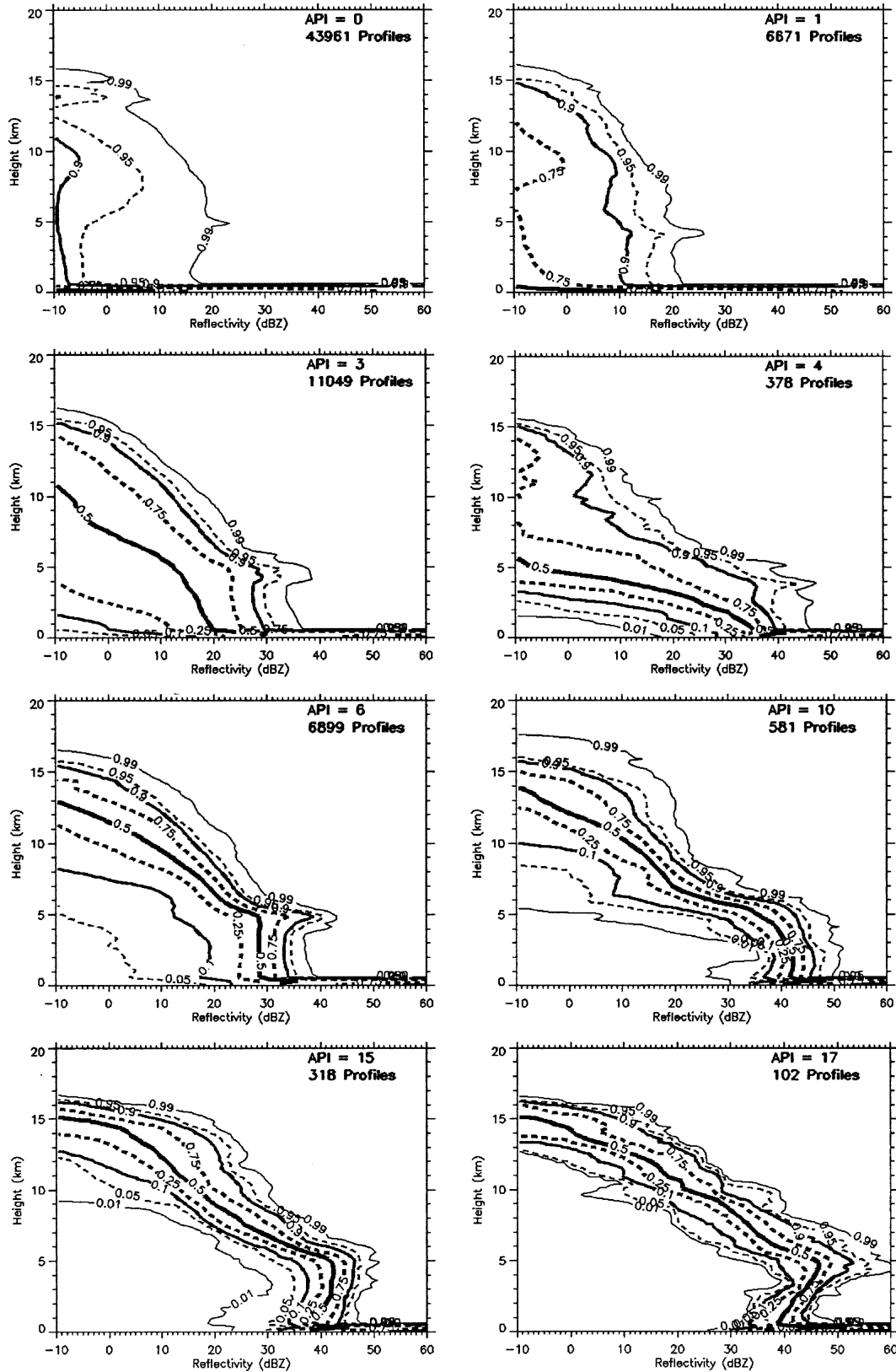
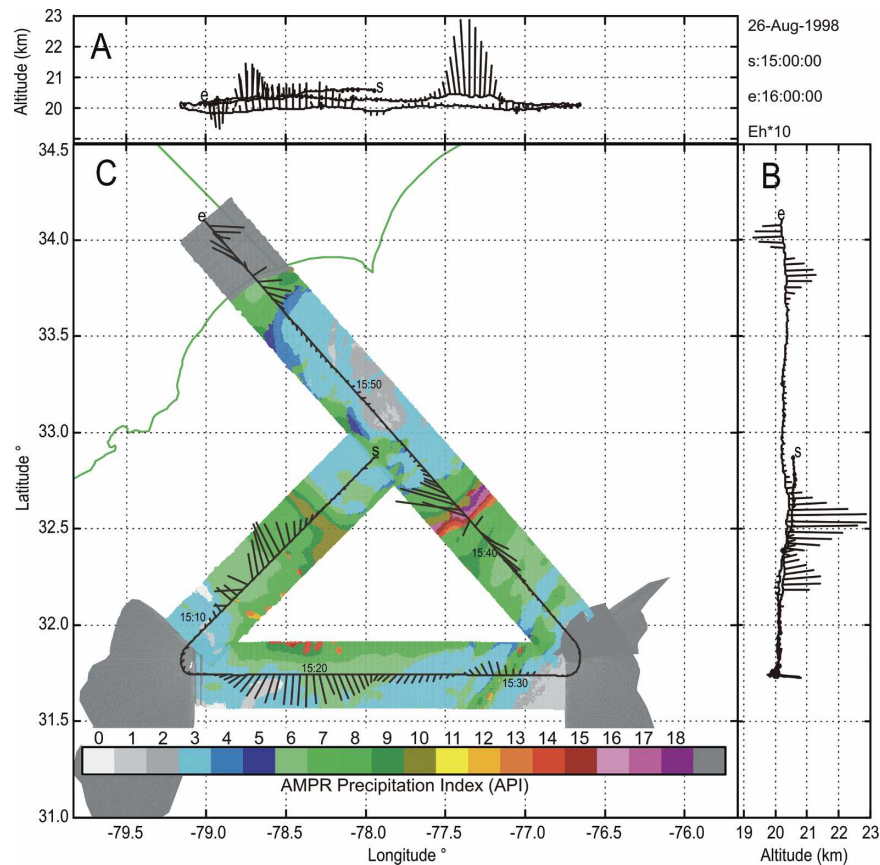FIG. 3. CDF of EDOP reflectivity as a function of height for selected API values.

FIG. 4. Horizontal mapping of API and projections of 3D electric field and aircraft location onto (a) longitude–altitude plane, (b) latitude–altitude plane, and (c) longitude–latitude plane. The "S" denotes start of aircraft track (1500 UTC), and the "e" denotes end of aircraft track (1600 UTC). API color scale is shown. Electric field and aircraft location are plotted as if projected onto three sides of a box. The projections of the electric field onto (a)–(c) are plotted as barbs originating at the aircraft location. A barb extending 2 km above the aircraft track denotes a +1 kV m^{-1} (positive charge below the aircraft) electric field. Note that the vertical component dominates the longitudinal and latitudinal components of electric field in (a) and (b). Barb lengths are scaled by a factor of 10 in (c) because the horizontal components of the electric field are so small.

negative charges) areas of charge. Note, while the low sample interval employed in Fig. 4 provides an excellent picture of the quasi-steady charge distributions in the clouds overflown, details of the transient field changes associated with lightning exist but are not shown.

To quantify relationships between API and cloud electrification, Table 2 summarizes the measured elec-

TABLE 2. Number of occurrences of weak, medium, and strong vertical electric fields as a function of the maximum API value in the vicinity. Taken from subjective analysis of 11 tropical cyclone and three noncyclone aircraft missions. Analysis of electrification tends to be weak when the 37.1-GHz channel is not scattered. There usually is significant electrification when the 37.1-GHz channel is scattered and strong electrification when the 19.35-GHz channel is scattered.

API	Weak <50 V m^{-1}	Medium 50–1000 V m^{-1}	Strong >1000 V m^{-1}	API summary
9–10	7	9	0	Heavy rain with only 85.5-GHz scattering
12	2	4	0	Moderate rain with 85.5- and 37.1-GHz scattering
15	1	21	1	Heavy rain with 85.5- and 37.1-GHz scattering
18	0	11	13	Heavy rain with 85.5-, 37.1-, and 19.35-GHz scattering

tric fields in regions where the maximum API indicates different levels of emission or scattering. When the maximum API in a region indicates that all of our scattering tests have been met (85.5-, 37.1-, and 19.35-GHz channels are scattered), significant electric fields are always encountered. These fields are often rather strong, with values exceeding 1000 V m^{-1} measured at the aircraft altitude (20 km). When the higher frequency channels are scattered, but the 19.35-GHz channel is not, there is usually a substantial electric field, but not as strong as when the lower frequency channel is scattered. When only the 85.5-GHz channel is scattered, about half the cases have small or insignificant electric fields ($<50 \text{ V m}^{-1}$). Of the cases with substantial electric fields but without at least 37.0-GHz scattering, there are often indications that a stronger scattering core is located beyond the swath sampled by AMPR. That is, the electric field measurements sometimes suggest the location of strong convection that would otherwise go unnoticed by the aircraft. Table 2 is consistent with our expectations, and with the interpretation that the same strong updrafts that produce large ice and therefore scatter the microwave channels also produce the microphysical conditions of supercooled water, large ice, and bouncing collisions with smaller ice in which substantial electric charge is separated.

4. Hurricane Bonnie case

To demonstrate the relationships between the API, electric field, and radar reflectivity, a portion of the overflight of Hurricane Bonnie of 26 August 1998 is examined in detail. After becoming a hurricane on 22 August 1998 northeast of Hispaniola, Hurricane Bonnie made landfall near Wilmington, North Carolina, on the afternoon of 26 August as a category 2 storm (Pasch et al. 2001). The NASA ER-2 high-altitude aircraft (carrying AMPR, EDOP, LIP, and other instruments) performed multiple overpasses of Hurricane Bonnie from 1120–1720 UTC on 26 August. Diverse precipitation structures were observed, allowing us to illustrate many API, electric field, and radar characteristics in a single example. As mentioned in the previous section, the API and electric field vectors are mapped in Fig. 4 between 1500 and 1600 UTC. The ER-2 flight track begins with a radial leg from the eye to the southwest quadrant, then a downwind leg from west to east, and an overflight of the eye with an exit to the northwest over land. The ER-2 flight track is overlaid on a 1501 UTC reflectivity image from the NOAA-42 P-3 lower fuselage radar in Fig. 5. Figures 4 and 5 show similar horizontal structure, considering that the precipitation field advects and evolves during the 1-h flight pattern.

The greatest radar reflectivity values are seen in the western portion of the outer eyewall (not observed by this ER-2 flight segment but present in Fig. 5) and also in the southern and southeastern portions of the outer eyewall. The strongest electric fields and the largest API values (i.e., deepest and strongest convection) are observed while the ER-2 crosses the southeastern portion of the outer eyewall near 32.5°N, 77.4°W (Fig. 4). In the southwestern portion of this flight segment, enhanced API and electric fields suggest strong convection to the left of the flight track. Several lightning flashes are detected, although they are not apparent with the data resolution plotted in Fig. 4. The suggested location of strong convection is consistent with the NOAA P-3 reflectivity patterns in the southern portion of Fig. 5, where enhanced eyewall reflectivity and some banding are seen just outside the eyewall.

The southeast-to-northwest eyewall overpass in Fig. 4 is examined in further detail using Figs. 6, 7, 8, and 9. Consider the vertical cross section of reflectivity (Fig. 6), the vertical electric field and API (Fig. 7), nadir brightness temperatures (Fig. 8), and simulated radar reflectivity (Fig. 9) derived from the median reflectivity profiles for each API value in Fig. 2. At far left (southeast) in Fig. 7, API = 1 suggests nonprecipitating clouds. EDOP agrees, with only weak reflectivities (<0 dBZ) around 6 and 12 km altitude. Following the flight track, next the API increases to values of 6 to 8, indicating rain with moderate ice. Indeed, the EDOP measures >30 dBZ near the surface with >10 dBZ reflectivity extending about 3 km above the bright band. The local maximum of API = 8 (heavy rain, moderate ice) coincides with the local reflectivity maximum (>55 dBZ near the surface at $x = 22$ km). The moderate ice categories are barely triggered, with the 85.5-GHz TB only a few degrees Kelvin less than the 37.1-GHz TB (Fig. 8). Because the ice scattering criteria are only minimally met, the reflectivity simulated by API in Fig. 9 overestimates the vertical extent of precipitation in this region.

Continuing along the flight track, the API briefly decreases to 3 while reflectivity through the vertical column also decreases. The flight segment then encounters a thick anvil beginning around $x = 30$ km, with echo tops reaching 16 km, API returning to values of 6 and 7, and the vertical electric field becoming slightly negative. This excursion of the electric field may be due to a weak positively charged layer near the top of the anvil, which is only ~4 km below the aircraft.

API values between 6 and 9 vary with reflectivity in the rain layer. There is a close correspondence between API maxima (e.g., at $x = 47$ km; $x = 75$ km) and reflectivity maxima. The vertical electric field (E_z) be-
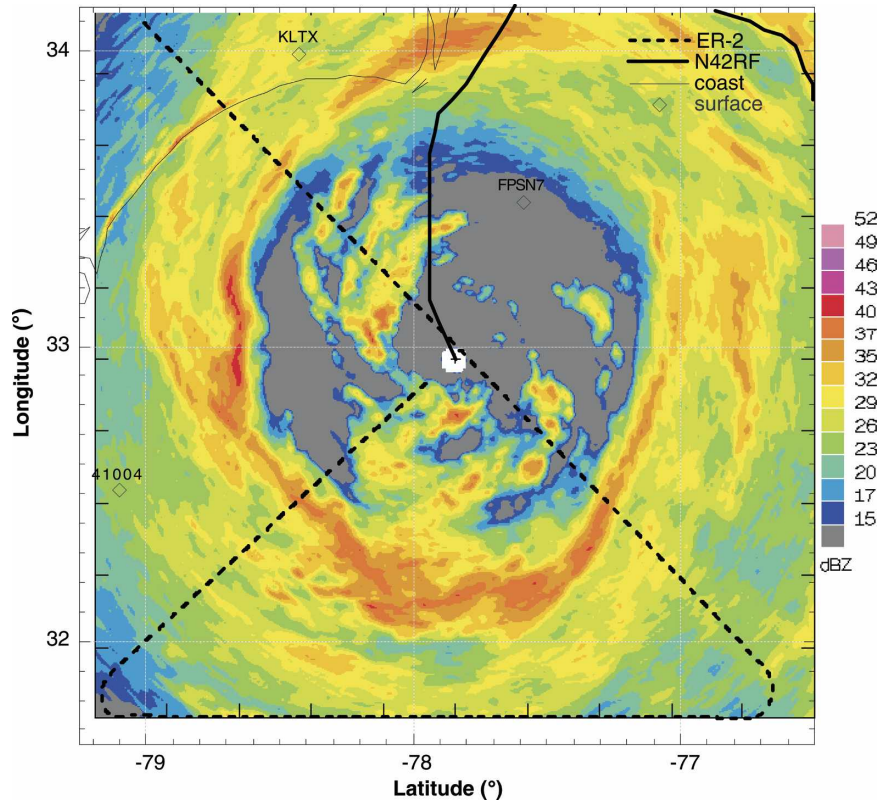
FIG. 5. Reflectivity scan from NOAA-42 lower-fuselage radar in eye of Hurricane Bonnie at 1500 UTC 26 Aug 1998. ER-2 flight track between 1500 and 1600 UTC is overlaid.

comes strongly positive and peaks at $x = 90$ km just before the eyewall reflectivity and scattering cores. This may be due to the sloping eyewall and the $20+$ km altitude of the Ez measurements. Peak Ez at flight level coincides with peak reflectivity at ~11–13 km altitude and the highest 10–20-dBZ echo tops. Then Ez decreases rapidly while the echo-top heights also decrease.

API increases to 14 and 15 (heavy rain with heavy ice) on the edge of the eyewall reflectivity core, and then increases to 16–18 (intense ice) over the core itself. This increase of API results from the lower frequency channels successively being scattered by larger graupel and/or hail. The peak 19.35-GHz scattering at $x = 92$ km is slightly offset from the peak 10.7-GHz emission at $x = 95$ km. This may be another result of the sloping eyewall, perhaps coupled with slight scattering in the 10.7-GHz channel at $x = 92$ km. The region with strongest electric field and most significant scattering also includes the strongest upper-level updrafts (Fig. 10). Future work will attempt to quantify this relationship.

Inward (further right in Figs. 6–10) from this outer eyewall is mostly shallow rain. Some of it is gla-

ciated, but having low reflectivities above the bright band with minimal AMPR ice scattering signatures (values less than 6). AMPR does detect the inner eyewall on the southeast side at $x = 150$ km, with API $= 7$. Clouds are indicated inside the eye, with API values of 1 and 2 at $x = 155$–185 km. This is consistent with our visual observations from the NASA DC-8 aircraft, which was flying with the ER-2 during this mission. API suggests a broad region of shallow, light rain between $x = 185$ and 250 km and fails to detect the deep ice layer above the northwest inner eyewall at $x = 200$–220 km. This feature is too weak for the API to handle properly; reflectivities are mostly below 20 dBZ both aloft and in the rain layer. There is a hint of 85.5-GHz scattering and some 37.1-GHz emission, but the algorithm requires more of either scattering or emission in order to trigger an ice index (i.e., API 6 or greater, with TB85 $<$ TB37). Consequently, the simulated reflectivity (Fig. 9) underestimates the vertical extent of this feature. Inclusion of a higher frequency channel (more sensitive to smaller ice) would likely help in situations such as this.

Between $x = 220$–250 km, the API correctly identifies the shallow (~2 km) rain on the inner edge of the
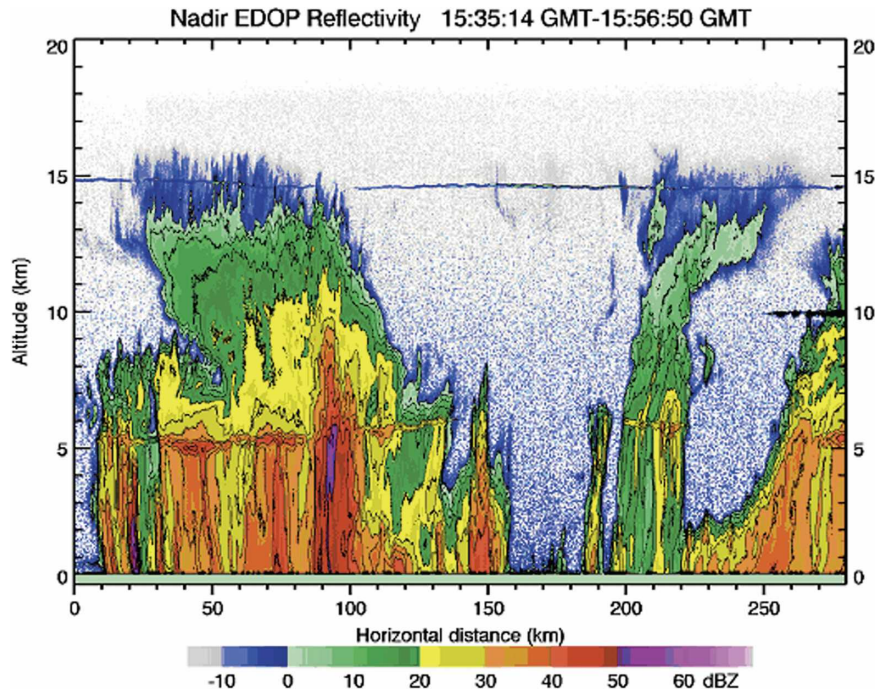
FIG. 6. Vertical cross section of nadir EDOP reflectivity, 1535–1557 UTC 26 Aug 1998. Cross section extends from (left) 170 km southeast of the center of Hurricane Bonnie to (right) 110 km northwest of the center. Contours every 5 dBZ; colors as in Fig. 9.

sloping outer eyewall. The identification by API is qualitatively correct, but the simulated reflectivity overestimates the depth of the rain and underestimates the magnitude of the rain. EDOP vertical velocities show a shallow eyewall updraft (Fig. 10); the ice scat-

tering design in the API is not particularly suited to detect this. On the far right (northwest side) of the cross section, the rain increases in both depth and magnitude as API increases from 3 to 4 and then to 8.

This cross section was chosen because it demon-
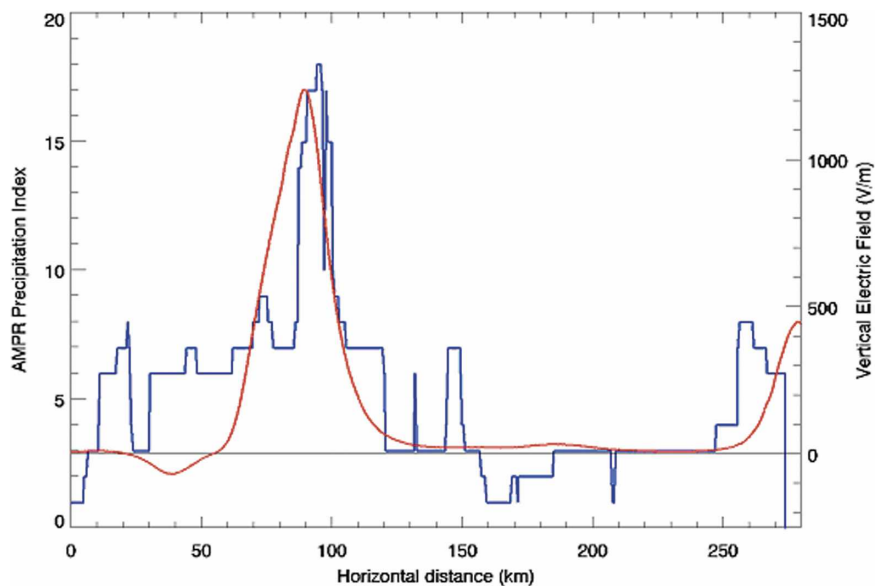
FIG. 7. Nadir API (blue) and the vertical component of electric field (red) coincident with Fig. 6.
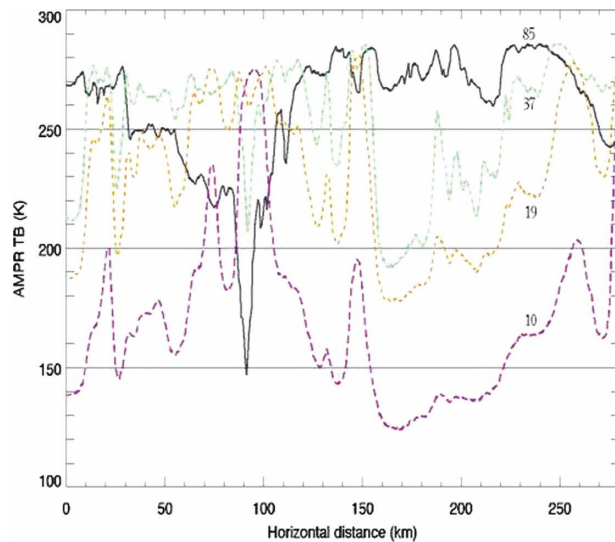
FIG. 8. Nadir AMPR brightness temperatures at 10.7, 19.35, 37.1, and 85.5 GHz coincident with Fig. 6.

strates a wide variety of vertical structures, and includes all but the least common API values. Comparing API with reflectivity in this example, API does behave as qualitatively intended with very few exceptions. The simulated reflectivity shows structure similar to that measured by EDOP along the southeastern radial (the left half of the cross section). In particular, the identification of localized rainfall maxima and the discrimination between different depths of precipitation is encouraging. The northwestern portion, particularly around $x = 200$–250 km, points out limitations of the API algorithm, as a deep layer of very light rain and ice is not distinguished from a shallow layer of heavier rain.

We are encouraged by the similarities between the simulated reflectivity in Fig. 9 and the observed reflectivity in Fig. 6 for the southeastern (left) portions of the flight line. The retrieval of the detailed vertical structure given only four passive microwave channels is an ill-posed problem. There are many uncertainties associated with the vertical structure, the distribution of water mass between liquid and ice phases, and the distributions of particle sizes and densities. Additional channels would likely remove only some of this uncertainty. A higher frequency channel (e.g., ~150 GHz) should improve the ability to recognize the deep layers of light rain in the northwest eyewall region ($x \simeq 200$ km), for example. But at best, our goal is to provide a general picture of the three-dimensional precipitation structure given a limited set of measurements.

5. Summary

An oceanic precipitation screening technique that combines the information content of the four AMPR
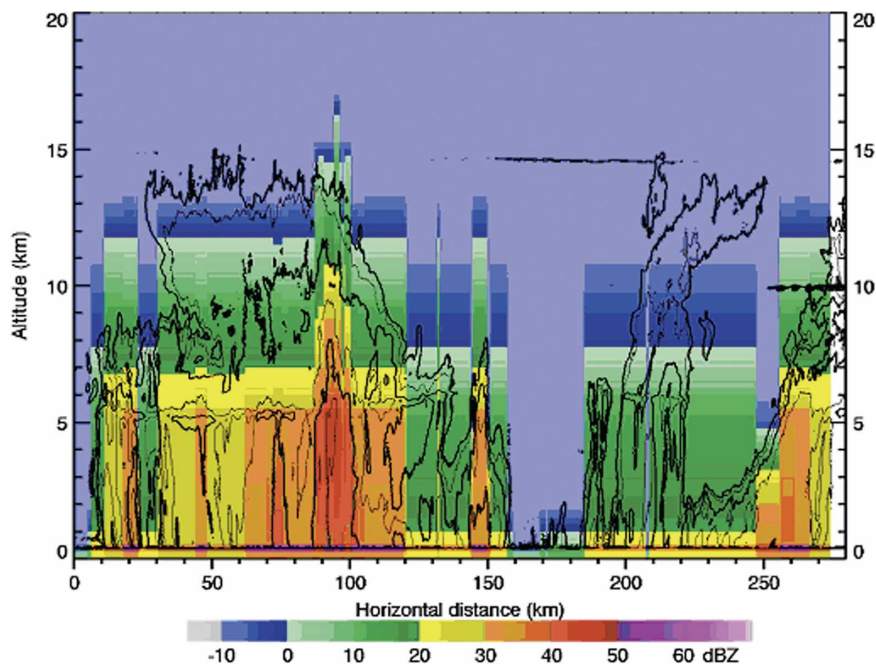

FIG. 9. Radar reflectivity simulated by API, coincident with Fig. 6. Simulated reflectivity is the convolution of observed API in Fig. 7 and the median reflectivity profiles in Fig. 2. Black contours are measured EDOP reflectivity from Fig. 6.
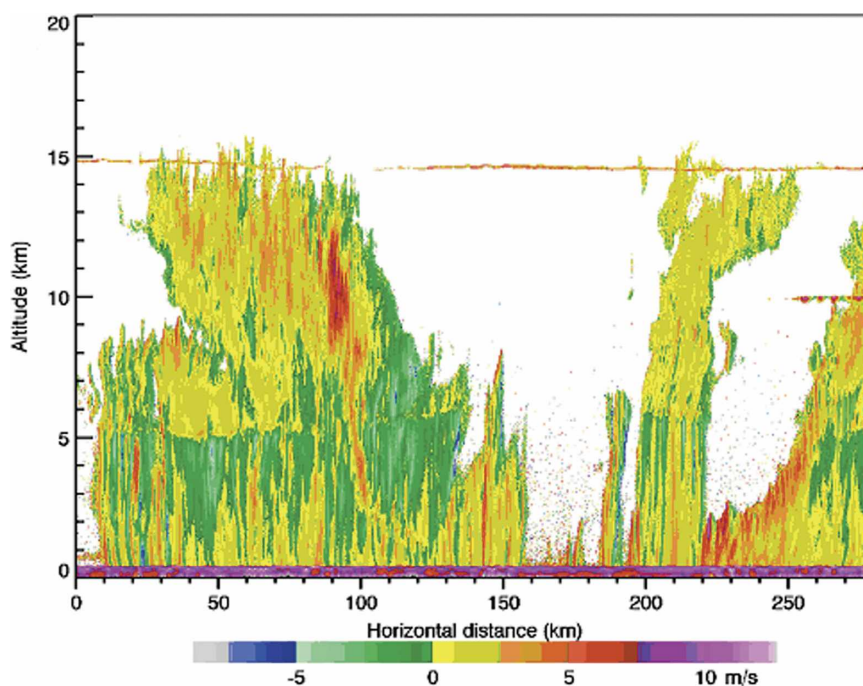
FIG. 10. Vertical cross section of nadir EDOP vertical velocity coincident with Fig. 6. Hydrometeor fall speeds removed following Heymsfield et al. (1999).

frequencies at a given data pixel into one precipitation index is presented. The technique, which has been verified with EDOP and NOAA P-3 data, shows promise as a computationally and conceptually easy rainfall mapping tool suitable for application to high spatial and temporal resolution airborne data. While more sophisticated approaches may yield more accurate retrievals, strength of the API is that any measurement can be quickly related to the physical concepts of microwave emission by rain and scattering by ice.

The 10.7-GHz brightness temperatures are successfully used to stratify measurements according to their low-level rain rates. API values requiring successively higher 10.7-GHz brightness temperatures in Table 1 have successively greater low-level radar reflectivity and derived rain rate in Fig. 2 and Table 1. These low-level reflectivities and rain rates for a given 10.7-GHz threshold are not substantially different from each other for API values that have different ice scattering signature characteristics (e.g., comparing API values 4, 7, and 12). The scattering of one channel relative to another is successfully used to stratify measurements according to their convective intensity and ice content aloft. API values requiring scattering of lower frequencies in Table 1 have successively greater radar reflectivity aloft and derived ice content in Fig. 2 and Table 1. The ice scattering tests also successfully discriminate between regions that are likely to be strongly electri-

fied, moderately electrified, and weakly electrified (Table 2). The API values with 19.35-GHz scattering virtually always coincide with substantial electrification, and the electric fields are often quite strong (>1000 V m^{-1}). The API values with 37.1-GHz scattering (but not 19.35-GHz scattering) rarely have such strong electric fields (>1000 V m^{-1}), but also rarely have weak electric fields (<50 V m^{-1}).

Further study using this type of analysis will examine the other CAMEX precipitation cases to quantify the relationship between lightning and microwave information as a surrogate indicator of convective strength. A more extensive examination of the NOAA P-3 radar information and the CAMEX microphysical data will be conducted to explore the feasibility of adding a rain-rate conversion algorithm to the API screening technique for use as quantitative precipitation estimation tool.

The synergy of the AMPR, EDOP, and LIP datasets has been presented here not only as a research tool for those interested in hurricane studies or as a validation tool for those developing satellite rainfall algorithms, but also as an example of how airborne information may be merged into real-time observational products. Future concepts for earth observation include adding airborne platforms such as uninhabited aerial vehicles or ultralong duration balloons into a mixture of spaceborne and surface-based assets comprising a flexible,

adaptive global observation network. Within these types of frameworks, an airborne vehicle could be positioned to provide high spatial and temporal resolution coverage of a critical weather event in concert with spaceborne and surface instrumentation so that the best combination of information is used for observation and prediction of the event outcome. As technical development of airborne platforms for this type of use progresses, appropriate airborne instrumentation and data algorithms should be identified that provide the maximum amount of information using the most feasible airborne payload for a given application. This study presents instrument candidates that could be used for high-altitude monitoring of precipitation type and convective strength for tropical cyclone and other precipitation systems. The research and operational communities should also examine many other types of instruments and flight altitudes in order to choose the optimal mixture of observations.

REFERENCES

Blakeslee, R. J., H. J. Christian, and B. Vonnegut, 1989: Electrical measurements over thunderstorms. *J. Geophys. Res.,* **94,** 13 135–13 140.

Cecil, D. J., and E. J. Zipser, 1999: Relationships between tropical cyclone intensity and satellite-based indicators of inner core convection: 85-GHz ice-scattering signature and lightning. *Mon. Wea. Rev.,* **127,** 103–123.

——, and ——, 2002: Reflectivity, ice scattering, and lightning characteristics of hurricane eyewalls and rainbands. Part II: Intercomparison of observations. *Mon. Wea. Rev.,* **130,** 785–801.

Evans, K. F., J. Turk, T. Wong, and G. L. Stephens, 1995: A Bayesian approach to microwave precipitation profile retrieval. *J. Appl. Meteor.,* **34,** 260–279.

Ferraro, R. R., E. A. Smith, W. Berg, and G. J. Huffman, 1998: A screening methodology for passive microwave precipitation retrieval algorithms. *J. Atmos. Sci.,* **55,** 1583–1599.

Gunn, R., and J. P. Parker, 1946: The high-voltage characteristics of aircraft in flight. *Proc. IRE,* **34,** 241–247.

Heymsfield, G. M., I. J. Caylor, J. M. Shepherd, W. S. Olson, S. W. Bidwell, W. C. Boncyk, and S. Ameen, 1996: Structure of Florida thunderstorms using high-altitude aircraft radiometer and radar observations. *J. Appl. Meteor.,* **35,** 1736–1762.

——, J. B. Halverson, and I. J. Caylor, 1999: A winter time Gulf Coast squall line observed by EDOP airborne Doppler radar. *Mon. Wea. Rev.,* **127,** 2928–2950.

——, ——, J. Simpson, L. Tian, and T. P. Bui, 2001: ER-2 Doppler radar investigations of the eyewall of Hurricane Bonnie during the Convection and Moisture Experiment-3. *J. Appl. Meteor.,* **40,** 1310–1330.

Hong, Y., J. L. Haferman, W. S. Olson, and C. D. Kummerow, 2000: Microwave brightness temperatures of tilted convective systems. *J. Appl. Meteor.,* **39,** 983–998.

Iguchi, T., and R. Meneghini, 1994: Intercomparison of single-frequency methods for retrieving a vertical rain profile from airborne or spaceborne radar data. *J. Atmos. Oceanic Technol.,* **11,** 1507–1516.

Jorgensen, D. P., and P. T. Willis, 1982: A Z–R relationship for hurricanes. *J. Appl. Meteor.,* **21,** 356–366.

Kakar, R., M. Goodman, R. Hood, and A. Guillory, 2006: Overview of the Convection and Moisture Experiment (CAMEX). *J. Atmos. Sci.*, **63,** 5–18.

Kummerow, C., W. S. Olson, and L. Giglio, 1996: A simplified scheme for obtaining precipitation and vertical hydrometeor profiles from passive microwave sensors. *IEEE Trans. Geosci. Remote Sens.,* **34,** 1213–1232.

Mach, D. M., and W. J. Koshak, 2003: General matrix inversion technique for the calibration of electric field sensor arrays on aircraft platforms. Preprints, *12th Int. Conf. on Atmospheric Electricity*, Versailles, France, International Commission on Atmospheric Electricity, 207–210.

Marks, F. D., Jr., 1985: Evolution of the structure of precipitation in Hurricane Allen (1980). *Mon. Wea. Rev.,* **113,** 909–930.

McGaughey, G., E. J. Zipser, R. W. Spencer, and R. E. Hood, 1996: High-resolution passive microwave observations of convective systems over the tropical Pacific Ocean. *J. Appl. Meteor.,* **35,** 1921–1947.

Molinari, J., P. Moore, and V. Idone, 1999: Convective structure of hurricanes as revealed by lightning locations. *Mon. Wea. Rev.,* **127,** 520–534.

Olson, W. S., Y. Hong, C. D. Kummerow, and J. Turk, 2001: A texture-polarization method for estimating convective-stratiform precipitation area coverage from passive microwave radiometer data. *J. Appl. Meteor.,* **40,** 1577–1591.

Orville, R. E., and Coauthors, 1997: Lightning in the region of the TOGA COARE. *Bull. Amer. Meteor. Soc.,* **78,** 1055–1067.

Pasch, R. J., L. A. Avila, and J. L. Guiney, 2001: Atlantic hurricane season of 1998. *Mon. Wea. Rev.,* **129,** 3085–3123.

Simpson, J., J. B. Halverson, B. S. Ferrier, W. A. Petersen, R. H. Simpson, R. Blakeslee, and S. L. Durden, 1998: On the role of "hot towers" in tropical cyclone formation. *Meteor. Atmos. Phys.,* **67,** 15–35.

Skofronick-Jackson, G. M., J. R. Wang, G. M. Heymsfield, R. Hood, W. Manning, R. Meneghini, and J. A. Weinman, 2003: Combined radiometer–radar microphysical profile estimations with emphasis on high-frequency brightness temperature observations. *J. Appl. Meteor.,* **42,** 476–487.

Smith, E. A., X. Xiang, A. Mugnai, R. E. Hood, and R. W. Spencer, 1994: Behavior of an inversion-based precipitation retrieval algorithm with high-resolution AMPR measurements

including a low-frequency 10.7 GHz channel. *J. Atmos. Oceanic Technol.,* **11,** 858–873.

Spencer, R. W., H. M. Goodman, and R. E. Hood, 1989: Precipitation retrieval over land and ocean with the SSM/I: Identification and characteristics of the scattering signal. *J. Atmos. Oceanic Technol.,* **6,** 254–273.

——, R. E. Hood, F. J. LaFontaine, E. A. Smith, R. Platt, J. Galliano, V. L. Griffin, and E. Lobl, 1994: High resolution imaging of rain systems with the Advanced Microwave Precipitation Radiometer. *J. Atmos. Oceanic Technol.,* **11,** 849–857.

Wilheit, T. T., 1986: Some comments on passive microwave measurement of rain. *Bull. Amer. Meteor. Soc.,* **67,** 1226–1232.

——, A. T. Chang, M. S. V. Rao, E. B. Rodgers, and J. S. Theon, 1977: A satellite technique for quantitatively mapping rainfall rates over the oceans. *J. Appl. Meteor.,* **16,** 551–560.

——, J. L. King, E. B. Rodgers, R. A. Nieman, B. M. Krupp, A. S. Milman, J. S. Stratigos, and H. Siddalingaiah, 1982: Microwave radiometric observations near 19.35, 92, and 183 GHz of precipitation in Tropical Storm Cora. *J. Appl. Meteor.,* **21,** 1137–1145.

Winn, W. P., 1993: Aircraft measurement of electric field: Self-calibration. *J. Geophys. Res.,* **98,** 6351–6365.

Wu, J., and J. A. Weinman, 1984: Microwave radiances from precipitating clouds containing aspherical ice, combined phase, and liquid hydrometeors. *J. Geophys. Res.,* **89,** 7170–7178.